International Journal of Solids and Structures 51 (2014) 3866–3877

Contents lists available at ScienceDirect

International Journal of Solids and Structures

journal homepage: www.elsevier.com/locate/ijsolstr

The stiffness and strength of the gyroid lattice

S.N. Khaderi *, V.S. Deshpande, N.A. Fleck *

Department of Engineering, Cambridge University, Cambridge, United Kingdom

ARTICLE INFO

Article history:
Received 5 April 2013
Received in revised form 30 January 2014
Available online 17 July 2014

Keywords:
Gyroid lattice
Lattice materials
Foams

ABSTRACT

Recently, a nanoscale lattice material, based upon the gyroid topology has been self-assembled by phase separation techniques (Scherer et al., 2012) and prototyped in thin film applications. The mechanical properties of the gyroid are reported here. It is a cubic lattice, with a connectivity of three struts per joint, and is bending-dominated in its elasto-plastic response to all loading states except for hydrostatic: under a hydrostatic stress it exhibits stretching-dominated behaviour. The three independent elastic constants of the lattice are determined through a unit cell analysis using the finite element method; it is found that the elastic and shear modulus scale quadratically with the relative density of the lattice, whereas the bulk modulus scales linearly. The plastic collapse response of a rigid, ideally plastic gyroid lattice is explored using the upper bound method, and is validated by finite element calculations for an elastic-ideally plastic lattice. The effect of geometrical imperfections, in the form of random perturbations to the joint positions, is investigated for both stiffness and strength. It is demonstrated that the hydrostatic modulus and strength are imperfection sensitive, in contrast to the deviatoric response. The macroscopic yield surface of the imperfect lattice is adequately described by a modified version of Hill's anisotropic yield criterion. The article ends with a case study on the stress induced within a gyroid thin film, when the film and its substrate are subjected to a thermal expansion mismatch.

1. Introduction

Lattice materials are micro-architectured porous solids, and can be manufactured with a broad range of micro-structures and length scales. They can be random or periodic, and open or closed-cell. Examples include foams, the octet truss, hollow truss, gyroid, Kagome and honeycomb (Deshpande et al., 2001; Jacobsen et al., 2007; Queheillalt and Wadley, 2005; Fleck et al., 2010; Cote et al., 2004; Scherer et al., 2012). Their mechanical properties (for example stiffness, strength and fracture toughness) depend upon the properties of the parent material, upon the relative density $\bar{\rho}$ (density of the lattice/density of the solid) and upon the geometry of the lattice. When a macroscopic strain is applied to a lattice, it can deform by a combination of bending, twisting and stretching of the struts. A bending-dominated lattice has a lower strength and stiffness than that of a stretching-dominated lattice for the same value of $\bar{\rho}$ (Deshpande et al., 2001; Ashby, 2006; Gibson and Ashby, 1997). It is the nodal connectivity, Z, (i.e. the number of struts joining at a node) that determines whether the lattice deforms in a bending or stretching-dominated mode. In 3D, the elastic modulus of a foam (for which $Z = 3$–4) scales quadratically with the $\bar{\rho}$, whereas the elastic modulus of an octet truss lattice (for which $Z = 12$) scales linearly with $\bar{\rho}$ (Deshpande et al., 2001). In contrast, the fracture toughness of the lattice need not depend upon the fracture toughness of the parent material (Fleck and Qiu, 2007).

Lattice materials have potential for use as thin films in electrical application. For example, films of thickness on the micron scale and comprising the gyroid lattice have been manufactured by phase separation techniques (Scherer et al., 2012). Possible applications include displays (by employing electrochromism) and electrodes for solar cells. The successful use of such devices will require a knowledge of the mechanical properties of such gyroid lattices. This motivates the current study: our aim is to determine the stiffness and strength of the gyroid lattice in both its ideal, periodic state and in an imperfect state where the nodes are randomly displaced.

1.1. The gyroid lattice

The gyroid lattice, at low relative density, can be idealised by a periodic framework of slender struts of circular cross-section, see Fig. 1. It belongs to the cubic space group $I4_132$. The location of the nodes, i.e. the lattice sites of the space group, are given by

* Corresponding authors.
E-mail addresses: snk34@cam.ac.uk (S.N. Khaderi), vsd20@cam.ac.uk (V.S. Deshpande), naf1@cam.ac.uk (N.A. Fleck).

http://dx.doi.org/10.1016/j.ijsolstr.2014.06.024
0020-7683/

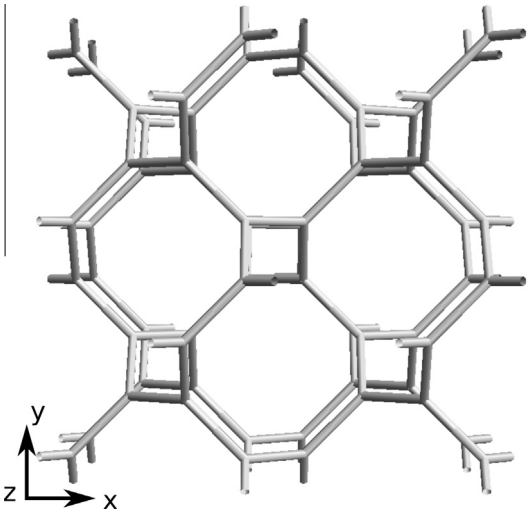

Fig. 1. A perspective view of the gyroid lattice.

Luzzati and Spegt (1967), for example. In the present study, we limit our attention to the gyroid lattice for which the struts are slender and the relative density $\bar{\rho}$ is below 4%. At $\bar{\rho} > 4\%$, the struts are stocky and vary significantly in cross-sectional shape and size along their length.

The main features of the lattice at $\bar{\rho} < 4\%$ are as follows: (i) it comprises struts that are arranged in a chiral fashion and (ii) it has a connectivity of three struts per node. The geometry, shown in Fig. 1, is also known as a 'single gyroid lattice'. When two single gyroids of opposite chirality interpenetrate each other, the resulting structure is known as a 'double gyroid', see for example Scherer (2009).

The unit cell of the gyroid lattice, with principal directions aligned with the Cartesian coordinate system (x, y, z), is shown in Fig. 2. It has twelve struts and eight nodes. The struts labelled 2, 4, 7 and 9 are aligned with the $x-y$ plane; the struts labelled 1, 3, 5, 6, 8 and 10 are aligned with the $y-z$ plane; and the struts labelled 11–17 are aligned with the $x-z$ plane. The unit tangential vector $\boldsymbol{t}$ for each strut is listed in Table 1. The length a of each side of the unit cell is related to the length of the strut L by $a = 2L\sqrt{2}$. The relative density of the gyroid lattice is

$$\bar{\rho} = \frac{3\pi}{16\sqrt{2}}\left(\frac{d}{L}\right)^2, \tag{1}$$

where d is the diameter of the struts. The above formula slightly over-estimates the value of relative density, because it double counts for material overlap at the nodes. The overall objective of this paper is to calculate the strength and stiffness of the gyroid lattice.

1.2. Natural and man-made gyroids

The gyroid morphology has been observed in many physical systems. For example, when strontium-saturated soaps are annealed at 230 °C, self-assembly of the lipids results in a double gyroid network of strontium ions embedded in a hydrocarbon matrix (Luzzati and Spegt, 1967). The double gyroid (DG) morphology also appears during the phase separation of diblock copolymers (see the review by Matsen and Bates (1996)). At high temperatures the block co-polymers exist as a disordered homogeneous solution; at low temperatures they phase separate/self assemble to form a variety of morphologies, which include lamellar, cylindrical, spherical and DG. The lowest energy configuration of these competing morphologies depends upon the volume fraction of each phase of the block co-polymers, interfacial energy and the entropic stretching energy of the polymer chains. The single gyroid network has been observed in the scales of butterfly wings. Michielsen and Stavenga (2008) compared the TEM images of the cross section of the scale of a butterfly wings with three different cubic micro-structures. They found that the gyroid lattice is the best fit to the TEM micro-structure. Saranathan et al. (2010) used small angle X-ray scattering to reveal that the micro-structure of the butterfly wings comprises the single gyroid lattice (unit cell size $\approx$ 300 nm). They also studied the optical properties of the gyroid lattice using photonic band gap modelling. Almsherqi et al. (2012) have shown that mitochondria of the retinal cone cells of tree shrew consist of the 8–12 parallel layers of gyroid surfaces (unit cell size $\approx$ 400 nm) that function as multi-focal lens, interference filter and wave guide.

On a macroscale, Yan et al. (2012) have fabricated macroscopic single gyroid lattices of $\bar{\rho} = 15\%$ from stainless steel powder using laser sintering technique. They also measured the stress–strain response of the gyroid lattices. As their main objective was to evaluate the laser sintering method to fabricate lattice materials, an extensive study on the mechanical properties was not performed. The bulk modulus of such high-relative density gyroid lattices has been calculated by Kapfer et al. (2011). However, the mode of deformation of individual strut (bending or stretching) was not identified.

Recently, Scherer et al. (2012) have shown that the annealing of poly(4-fluorostyrene-r-styrene)-b-poly(d,l-lactide) (P(F) S-b-PLA) results in a DG network of PLA embedded in styrene matrix. They successfully replaced the PLA with vanadium pentoxide and etched out the styrene matrix to obtain a DG of vanadium pentoxide (unit cell size $\approx$ 40 nm and $\bar{\rho} = 38\%$). This DG has potential for application in electrochromic devices.

Except for the work of Kapfer et al. (2011), very little is known about the mechanical properties of gyroid lattice and this is the subject of the present paper. The most common method to manufacture gyroids is via phase separation as mentioned in this section. Such techniques generate gyroids with a relative density around 20%. Empirical equations (Michielsen and Kole, 2003; Scherer et al., 2012) are typically used to approximate the geometry of these gyroids. However, these equations result in unrealistic geometry predictions in the low relative density regime. For example, the equation used by Scherer et al. (2012) predicts that gyroids will have struts of zero cross-sectional area for $\bar{\rho} < 2\%$. The aim of the current study is to investigate the properties of a low relative density cellular structure (that can be made by say 3D printing) with a gyroid topology, i.e. a cellular structure with nodes located in a gyroid-like spatial configuration but connected by slender struts of uniform cross-sectional area.

The paper is organised as follows. First, we extract the elastic constants of the gyroid lattice by performing a finite element analysis of the unit cell. Next, the yield surface of the gyroid is calculated analytically by the upper bound method and verified using finite element simulations.The effect of geometric imperfection on the elasto-plastic properties of the gyroid is then investigated: the nodes are moved in a random manner to generate imperfect gyroids. An analytical expression for the multi-axial yielding of the imperfect gyroid is proposed, and is employed in a case study on the yielding of a thin film, when subjected to a thermal expansion mismatch with the underlying substrate.

2. Elastic response of the gyroid lattice

Consider again the unit cell of the gyroid lattice as shown in Fig. 2. A periodic, unit cell analysis is performed using the finite element (FE) software (ABAQUS) in order to extract the effective

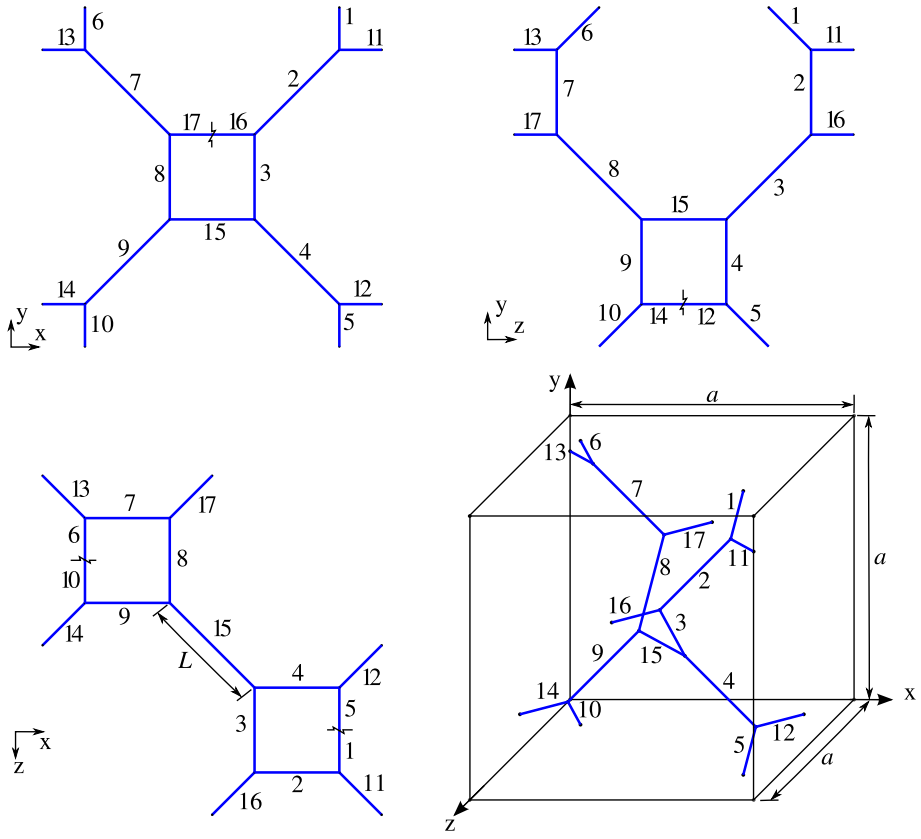

Fig. 2. Different views of the unit cell of the gyroid lattice. The struts are labelled as shown.

Table 1
Unit vector $\boldsymbol{t}$ along the struts of the gyroid lattice, as shown in Fig. 2. The unit vectors in the (x,y,z) directions are represented by $(\boldsymbol{e}_x, \boldsymbol{e}_y, \boldsymbol{e}_z)$.

Strut number	$\boldsymbol{t}$
1, 8, 5	$(\boldsymbol{e}_y - \boldsymbol{e}_z)/\sqrt{2}$
6, 3, 10	$(\boldsymbol{e}_y + \boldsymbol{e}_z)/\sqrt{2}$
2, 9	$(\boldsymbol{e}_x + \boldsymbol{e}_y)/\sqrt{2}$
4, 7	$(\boldsymbol{e}_x - \boldsymbol{e}_y)/\sqrt{2}$
12, 14, 16, 17	$(\boldsymbol{e}_x - \boldsymbol{e}_z)/\sqrt{2}$
11, 13, 15	$(\boldsymbol{e}_x + \boldsymbol{e}_z)/\sqrt{2}$

elastic properties. The struts of the lattice are modelled as linear Timoshenko beam elements (B31 in ABAQUS terminology). Each strut of the lattice is discretised into 16 elements (increasing the number of elements by a factor of 2 leads to a change in the FE results by less than 0.1%.).

The unit cell is subjected to periodic boundary conditions, such that the relative displacement Δu_i of periodic nodes of the FE mesh is given by $\Delta u_i = \epsilon_{ij}\Delta X_j$, in terms of an imposed macroscopic strain ϵ_{ij}, and the relative position of the periodic nodes in the j^{th} direction ΔX_j. The resulting macroscopic stress, σ_{ij}, is obtained from the reaction forces on the periodic nodes and is given by

$$\sigma_{ij} = \frac{1}{2a^3}\sum_J \left(\Delta X_i F_j^J + \Delta X_j F_i^J\right), \tag{2}$$

where F_j^J are the reaction forces on the node J, and summation is performed on all boundary nodes. All FE simulations reported in this work are based on a small deformation theory.

The parent solid material is isotropic, with elastic modulus E_S and Poisson ratio $\nu_S = 0.3$. Since the gyroid lattice has cubic symmetry (with x,y and z as cubic directions), its macroscopic elastic behaviour is governed by the uniaxial modulus E, the Poisson ratio ν and the shear modulus G. The relationship between the macroscopic stress σ_{ij} and strain ϵ_{ij}, in the cubic directions, is given by

$$\begin{pmatrix} \epsilon_{xx} \\ \epsilon_{yy} \\ \epsilon_{zz} \\ 2\epsilon_{yz} \\ 2\epsilon_{xz} \\ 2\epsilon_{xy} \end{pmatrix} = \begin{pmatrix} 1/E & -\nu/E & -\nu/E & 0 & 0 & 0 \\ -\nu/E & 1/E & -\nu/E & 0 & 0 & 0 \\ -\nu/E & -\nu/E & 1/E & 0 & 0 & 0 \\ 0 & 0 & 0 & 1/G & 0 & 0 \\ 0 & 0 & 0 & 0 & 1/G & 0 \\ 0 & 0 & 0 & 0 & 0 & 1/G \end{pmatrix} \begin{pmatrix} \sigma_{xx} \\ \sigma_{yy} \\ \sigma_{zz} \\ \sigma_{yz} \\ \sigma_{xz} \\ \sigma_{xy} \end{pmatrix}. \tag{3}$$

Recall that the bulk modulus K is related to (E,ν) according to $K = E/3(1-2\nu)$.

Three choices of ϵ_{ij} are made in the finite element simulations in order to extract the values for (E,G,K) for any given $\bar{\rho}$. The results are shown in Fig. 3, and the curve fits to these predictions are:

$$\begin{aligned} \frac{E}{E_s} &= 0.426\bar{\rho}^2, \\ \frac{G}{E_s} &= 0.329\bar{\rho}^2, \\ \frac{K}{E_s} &= \frac{1}{9}\bar{\rho}. \end{aligned} \tag{4}$$

The quadratic dependence of E and G upon the relative density indicates that the lattice deforms predominantly by bending of the struts for uniaxial tension and for shear of the lattice. In contrast, the bulk modulus has a linear dependence upon $\bar{\rho}$, signifying that the beam elements stretch under macroscopic hydrostatic loading.

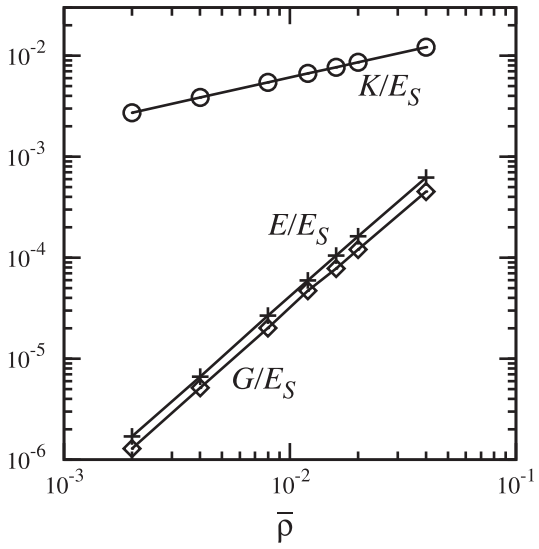

Fig. 3. Elastic constants of the gyroid lattice.

A similar behaviour has been reported for Kelvin foams (see for example Christensen (2000)). Consequently, $K/E \to \infty$ as $\bar{\rho} \to 0$, implying that the Poisson ratio ν approaches 0.5 as $\bar{\rho} \to 0$.

3. Multi-axial yield surface for the perfect lattice

The multi-axial yield behaviour of the gyroid lattice is now analysed, using the upper bound theorem of plasticity. In this section, we report the response for direct loading in plane stress, combined shear and axisymmetric loadings. Some additional yield surfaces are given in Appendix A for other stress states. The yield surfaces are obtained by postulating a set of kinematically admissible collapse modes, and the collapse stress is determined for each. These collapse modes are identified by performing periodic cell FE simulations. The strut material is assumed to be an isotropic, elastic-ideally plastic solid of Young's modulus E_S, Poisson ratio ν_S and yield strength σ_S. It yields in accordance with J_2 flow theory. We shall assume $\nu_S = 0.3$ and the yield strain $\epsilon_S \equiv \sigma_S/E_S$ equals 0.01.[1] The simulations are performed for $\bar{\rho} = 3.3\%$. The accuracy of the upper bound predictions is then also assessed by comparison with the limit load predictions from the FE calculations.

3.1. Plane stress response

Consider the gyroid lattice aligned with Cartesian axes (x, y, z) as shown in Fig. 2. In the FE analysis, proportional straining is imposed, $\epsilon_{xx} = \lambda\epsilon_{yy}$, with λ held fixed. Periodic boundary conditions are applied with all macroscopic stress components σ_{ij}, equal to zero except for $(\sigma_{xx}, \sigma_{yy})$.

The FE prediction for the collapse surface is plotted in Fig. 4, along with the observed collapse modes. There are three collapse modes (labelled as 1, 2 and 3), and they involve plastic hinge formation at various nodes of the lattice. In each case, the collapse mode is characterised by a single degree of freedom ϕ, the rotation of the struts about the plastic hinges. Consequently, each collapse mode is associated with a fixed value of $\lambda = \infty, 0, -1$ for modes 1, 2 and 3, respectively. Each mode is associated with a flat facet on the yield surface.

Consider each mode in turn. In mode 1, the struts 11, 12, 13, 14, 15, 16 and 17 rotate by an angle ϕ about the y axis to cause a macroscopic plastic strain of $\epsilon^p_{xx} = -\epsilon^p_{zz} = \phi/2$. Mode 2 is the same collapse mechanism as mode 1, but is rotated by $\pi/2$ in space about the z axis. In mode 2, the struts 1, 3, 5, 6, 8 and 9 rotate by an angle ϕ about the x axis to cause a macroscopic plastic strain of $\epsilon^p_{yy} = -\epsilon^p_{zz} = \phi/2$. Note that the lattice is plastically incompressible for modes 1 and 2. The work done by the applied forces in mode 1 and 2 are equal to $\sigma_{xx}(\phi/2)a^3$ and $\sigma_{yy}(\phi/2)a^3$, respectively. The energy dissipated at the plastic hinges in both modes is $8M_p\phi$, where the plastic moment is $M_p = \sigma_S d^3/6$ and σ_S is the yield strength of the parent material. By equating the energy dissipated to the work done by the external forces we obtain

$$\begin{aligned} &\sigma_{xx} = \pm\sigma_Y \quad \text{for mode 1,} \\ &\sigma_{yy} = \pm\sigma_Y \quad \text{for mode 2,} \end{aligned} \tag{5}$$

where

$$\sigma_Y = \frac{\sigma_S}{6\sqrt{2}}\left(\frac{d}{L}\right)^3 = 0.438\sigma_S\bar{\rho}^{3/2}. \tag{6}$$

In the above yield criteria, the plus (minus) symbol is used when ϕ is in the same (opposite) direction as shown in Fig. 4(a). σ_Y is the uniaxial yield strength of the lattice and scales with relative density $\bar{\rho}$ according to $\sigma_Y \propto \bar{\rho}^{3/2}$, as expected for a bending-dominated 3D lattice (Gibson and Ashby, 1997). The analytical formula in (6) for σ_Y is compared with finite element simulations as a function $\bar{\rho}$ in Fig. 5 for the perfect lattice; the agreement is excellent.

Now consider mode 3. Mode 3 is the same collapse mode as mode 1, but is rotated by $\pi/2$ in space about the x axis. The struts 2, 4, 7 and 9 rotate by an angle ϕ about the zaxis causing the macroscopic plastic strains: $\epsilon^p_{xx} = -\epsilon^p_{yy} = \phi/2$. The lattice is again plastically incompressible, and the yield criterion reads

$$\sigma_{xx} - \sigma_{yy} = \pm\sigma_Y. \tag{7}$$

The above analytical results are compared with finite element simulations in Fig. 4(b). The agreement is excellent except at the intersection of two modes. Here, the struts deform by a combination of stretching and rotation at the plastic hinges.

3.2. Shear response

The shear yield response of the gyroid lattice is now explored in $(\sigma_{xy}, \sigma_{xz})$ space. The FE simulations are performed on the periodic unit cell by specifying proportional straining such that $\epsilon_{xy} = \lambda\epsilon_{xz}$, and all other stress components, except for $(\sigma_{xy}, \sigma_{xz})$, are equal to zero. The collapse surface, as obtained from FE simulations, is shown in Fig. 6, together with the associated collapse modes. There are two collapse modes (labelled 4 and 5), both of which are governed by a single degree of freedom ϕ, the rotation of struts about the nodes. Each collapse mode is associated with a fixed value of λ (=1 for mode 4 and -1 for mode 5), thereby generating flat facets on yield surface.

In mode 4, the struts 6, 3 and 5 rotate about the plastic hinges by $(\boldsymbol{e}_y - \boldsymbol{e}_z)\phi$ and in mode 5, the struts 1, 8 and 10 rotate about the plastic hinges by $(\boldsymbol{e}_y + \boldsymbol{e}_z)\phi$, where $\boldsymbol{e}_x, \boldsymbol{e}_y$ and $\boldsymbol{e}_z$ are the unit vectors in x, y and z directions (see Fig. 6(a)). Consider first mode 4. The macroscopic plastic shear strains caused by rotation of the struts are $\epsilon^p_{xy} = \epsilon^p_{xz} = \phi/4$, and the work done by the external forces is

$$W_{\text{ext}} = (\sigma_{xy} + \sigma_{xz})\frac{\phi}{4}a^3. \tag{8}$$

The effective plastic rotation of the struts is $\phi\sqrt{2}$, and the energy dissipated at the plastic hinges is

$$W_{\text{plas}} = 4M_p\left(\phi\sqrt{2}\right). \tag{9}$$

Upon equating the external work and the energy dissipated we obtain the yield criterion for activation of collapse mode 4 as

[1] For computational reasons, the material is endowed with a very small strain hardening, as specified by a tangent modulus $h = 10^{-4}E_S$.

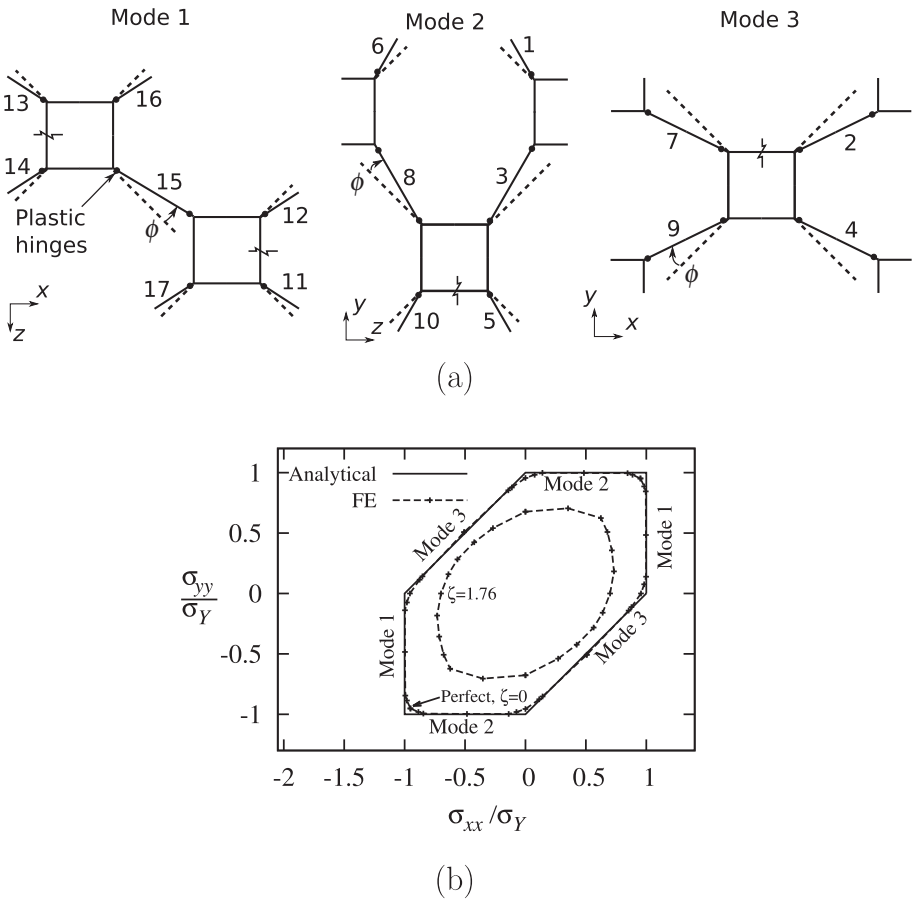

Fig. 4. Yield behaviour in $(\sigma_{xx}, \sigma_{yy})$ space. (a) Deformed geometry (solid lines) and location of plastic hinges for different modes of collapse. The dashed lines show the initial inclination of the struts. (b) Analytical and FE predictions of the yield surfaces with an indication of different modes of plastic collapse. The FE results are shown for perfect ($\zeta = 0$) and imperfect lattice with $\zeta = 1.76$.

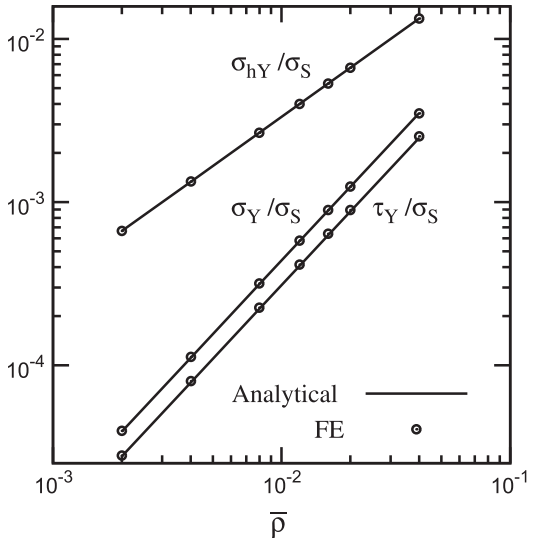

Fig. 5. Comparison of the uniaxial yield strength σ_Y, shear strength τ_Y and hydrostatic yield strength σ_{hY} obtained using FE simulations and upper bound theorem of plasticity. σ_S is the yield strength of the solid material.

$$\sigma_{xy} + \sigma_{xz} = \pm\frac{\sigma_Y}{\sqrt{2}}. \tag{10}$$

A similar calculation for mode 5 gives

$$\sigma_{xy} - \sigma_{xz} = \pm\frac{\sigma_Y}{\sqrt{2}}. \tag{11}$$

We conclude that the macroscopic shear strength of the lattice τ_Y is given by $\tau_Y = \sigma_Y/\sqrt{2}$. This value of τ_Y is compared with FE simulations in Fig. 5; the agreement is excellent. The analytical solutions in (10) and (11) are compared against finite element simulations for the perfect lattice in Fig. 6(b). The close agreement between the analytical and simulation results implies that the postulated upper bound collapse modes are exact.

3.3. Axisymmetric response

Next, assume the axisymmetric loading state $(\sigma_{xx} = \sigma_{yy}, \sigma_{zz})$, with other $\sigma_{ij} = 0$. This stress state arises, for example, when a thin film of gyroid lattice is thermally cycled on a substrate, with the unit normal to the free surface of the film aligned with the cubic z direction. The FE simulations are performed on the periodic unit cell by imposing proportional straining such that $\epsilon_{zz} = \lambda\epsilon_{xx}$, and the so-obtained yield surface is given in Fig. 7 along with the collapse mode (labelled as mode 6). The collapse mode consists of combined plastic rotation and axial stretching at nodes. It is instructive to consider two extreme cases. (1) When $\sigma_{xx} = \sigma_{zz}$, the lattice is in a state of hydrostatic stress, and the beam elements deform by axial stretching (as noted above for the elastic case). (2) When $\sigma_{zz} = 0$, the lattice is in a state of plane stress, where the lattice deforms both by a combination of hinge rotation and stretching, as noted above.

In the single collapse mode for axisymmetric loading, all struts except 2, 4, 7 and 8 yield plastically (see Fig. 7(a)). The collapse mode can be described by two degrees of freedom: the axial

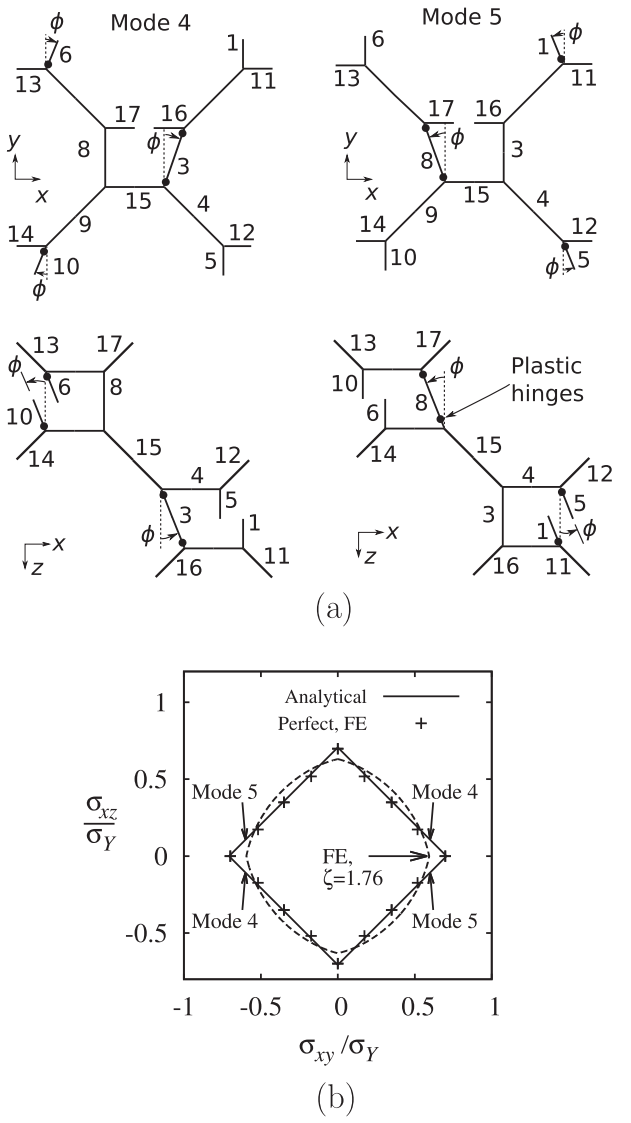

Fig. 6. Yield behaviour in $(\sigma_{xy}, \sigma_{xz})$ space. (a) Deformed geometry (solid lines) of gyroid and the locations of plastic hinges for different modes of collapse. (b) Comparison of analytical yield surface with FE predictions for the perfect ($\zeta = 0$) and imperfect gyroid with $\zeta = 1.76$.

extension $\epsilon L/2$ and rotation ϕ of the struts at the plastic hinges. Here, ϵ is a dimensionless kinematic variable characterising the degree of axial stretch. The collapse mode results in the following macroscopic plastic strains: $\epsilon^p_{xx} = \epsilon^p_{yy} = (\epsilon + \phi)/2$ and $\epsilon^p_{zz} = \epsilon - \phi$. Note that the extensional degree of freedom leads to dilatation of the unit cell, whereas the rotational degree of freedom results in a volume-preserving plastic strain. The work done by the external forces is

$$W_{\text{ext}}(\epsilon, \phi) = a^3(\sigma_{xx}(\epsilon + \phi) + \sigma_{zz}(\epsilon - \phi)).$$

The energy dissipated is given by

$$W_{\text{plas}}(\epsilon, \phi) = 16\frac{\epsilon L}{2}P_p(\xi) + 16\phi M_p(\xi), \tag{12}$$

where the plastic collapse force is $P_p(\xi) = \sigma_S d^2\left(\sin^{-1}\xi + \xi\sqrt{1-\xi^2}\right)/2$ and the plastic collapse moment is $M_p(\xi) = \sigma_S d^3\left(1-\xi^2\right)^{3/2}/6$. The neutral axis of bending/stretching of the plastic hinge is located at ξr, above the mid-plane of circular section (of radius r). A straightforward kinematic argument gives $\xi = (L/2r)(\epsilon/\phi)$. When $|\xi| > 1$, the neutral axis is located outside the beam with $M_p = 0$.

Now use the upper bound theorem and note that ϕ and ϵ are independent. Then, the macroscopic yield surface of the lattice for axisymmetric loading is obtained in parametric form as

$$\begin{aligned}\sigma_{xx} &= \frac{\sigma_Y}{2}\left[\frac{3}{2}\left(\frac{L}{d}\right)\left(\sin^{-1}\xi + \xi\sqrt{1-\xi^2}\right) \pm \left(1-\xi^2\right)^{3/2}\right],\\ \sigma_{zz} &= -\frac{\sigma_Y}{2}\left[-\frac{3}{2}\left(\frac{L}{d}\right)\left(\sin^{-1}\xi + \xi\sqrt{1-\xi^2}\right) \pm \left(1-\xi^2\right)^{3/2}\right],\end{aligned} \tag{13}$$

where $-1 \leqslant \xi \leqslant 1$. Upon making the choice $\xi = 1$ in (13), the hydrostatic limit is attained such that each direct stress is of magnitude

$$\sigma_{hY} = \frac{1}{3}\sigma_S\bar{\rho}. \tag{14}$$

Note that the hydrostatic strength scales linearly with the relative density $\bar{\rho}$, implying that the lattice deforms by axial stretching. This value of σ_{hY} is compared with FE simulations in Fig. 5; the agreement is excellent. The yield criterion as defined in (13) is exact for a rigid, ideally plastic solid and is confirmed by comparison with FE simulations in Fig. 7(b) for the perfect lattice. Recall that the uniaxial yield strength σ_Y scales as $\bar{\rho}^{3/2}$, thus the yield surface in Fig. 7(b) is increasingly elongated with diminishing $\bar{\rho}$.

Elastic buckling – The above analysis assumes that the gyroid lattice plastically collapses under hydrostatic loading. An

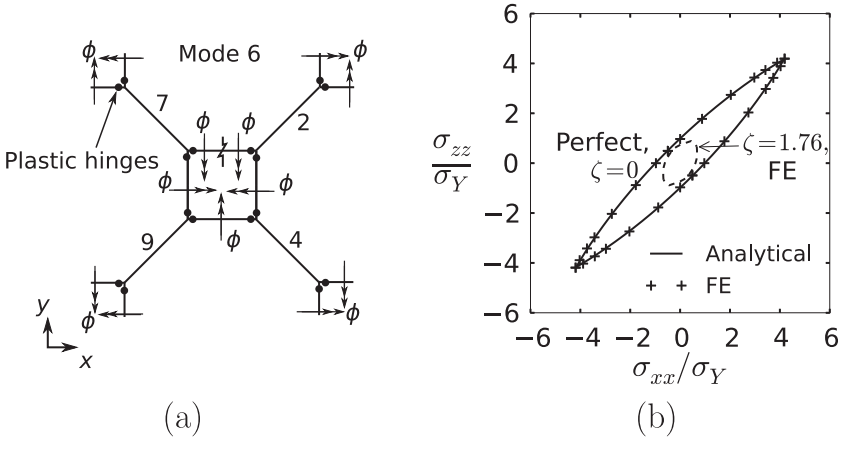

Fig. 7. Yield behaviour for axisymmetric loading ($\sigma_{xx} = \sigma_{yy}, \sigma_{zz}$). (a) Location of plastic hinges when the gyroid lattice is subjected to an axisymmetric load. (b) Comparison of analytical yield surface with FE simulations for perfect ($\zeta = 0$) lattice. The yield surface of imperfect lattice is labelled as $\zeta = 1.76$.

alternative possible collapse mode is elastic buckling. An elastic eigenvalue analysis has been performed using the FE software ABAQUS for the beam model. The simulations (not shown) reveal that the hydrostatic buckling strength is

$$\sigma_{\text{buckling}} = \frac{1}{13} E_s \bar{\rho}^2. \tag{15}$$

The switch in mechanism from plastic collapse to buckling occurs when the relative density $\bar{\rho}$ satisfies

$$\bar{\rho} = \frac{13}{3}\epsilon_S,$$

where $\epsilon_S = \sigma_S/E_S$ is the uniaxial yield strain of the parent material. For metals, typically, ϵ_S is less than 0.1%. Hence, elastic buckling will take place for $\bar{\rho} < 0.43\%$.

Since the lattice deforms by axial stretching under pure hydrostatic compression, the elastic bifurcation from the undeformed state can occur only for this stress state, see Chen et al. (1999). For other states of stress the lattice deforms by bending of struts, and the elastic bifurcation can happen only from a deformed configuration (see Papka and Kyriakides (1994) and Triantafyllidis and Schraad (1998) for a similar discussion on the bifurcation of hexagonal honeycombs). Consequently, to analyse the instabilities under these stress states, we have to perform a bifurcation analysis on the deformed configuration. Here we limit our attention to infinitesimal deformations, and thus a complete analysis of such instabilities is beyond the scope of the present work. We note in passing that no bifurcations (for any stress state) from the initial configuration are possible for the imperfect gyroid considered subsequently.

4. Effect of imperfections upon the elastic and plastic properties

Practical gyroid lattices contain a range of imperfections from spatial variations in relative density to missing beam elements and misplaced nodes. The significance of such imperfections has been explored for both 2D and 3D lattices, see for example (Silva et al., 1995; Chen et al., 1999; Zhu et al., 2000). We observe that the gyroid lattice shares several features with the 2D honeycomb: under deviatoric loading, the response is bending dominated whereas under hydrostatic loadings the beam elements stretch. For such lattices, the hydrostatic strength is much more imperfection-sensitive than the deviatoric strength. Is this a feature of the gyroid lattice too? In order to address this, the sensitivity of the elastic and plastic responses of the gyroid lattice is explored for the case where each node is displaced by a fixed distance ζd in a random direction, where d is the strut diameter and the imperfection magnitude ζ is taken to lie in the range of 0–2.

A FE analysis is performed on a periodic, representative volume element (RVE) containing $N^{1/3}$ unit cells along each of the Cartesian (x, y, z) axes. A convergence study is performed to determine the magnitude of the RVE that gives accurate macroscopic values for the elastic and plastic responses. Accordingly, the uniaxial modulus E and uniaxial yield strength σ_Y, as obtained from FE simulations, are plotted for various values of N in Fig. 8, for $\zeta = 0.353$. In the figure, E and σ_Y of the imperfect lattice are normalised by the responses of an ideal lattice (denoted by the superscript P). For each value of N, 5 random realizations are used. It can be seen that the results are independent of N provided $N \geqslant 64$. In the following we adopt this value for N.

4.1. Imperfection sensitivity

An assessment of the imperfection sensitivity of the main elastic and plastic properties of the lattice is now given. The uniaxial modulus E, shear modulus G and bulk modulus K (in material axes aligned with the Cartesian reference frame) are given in Fig. 9(a) for the choice $\bar{\rho} = 3.3\%$ and imperfection ζ in the range 0–1.76. Likewise, the uniaxial yield strength σ_Y, shear yield strength τ_Y and hydrostatic yield strength σ_{hY} are plotted as a function of $\bar{\rho}$ in Fig. 9(b). The values of E, G, σ_Y and τ_Y are almost insensitive to the level of imperfection ζ, whereas the bulk modulus K and the hydrostatic yield strength σ_{hY} are extremely imperfection sensitive. This can be explained as follows. The deformation mode changes from stretching to bending when a small imperfection is introduced. The dependence of K on $\bar{\rho}$ then changes from linear to quadratic; similarly, the scaling of σ_{hY} changes from linear to 3/2 power.

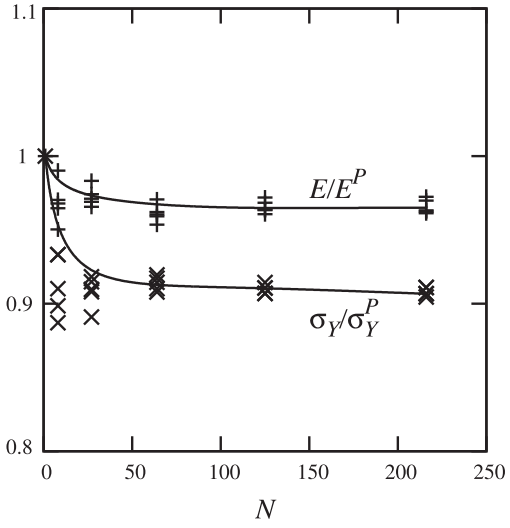

Fig. 8. Dependence of the uniaxial modulus E and yield strength σ_Y of an imperfect gyroid on the number of cells (N) used for $\zeta = 0.353$. The superscript P denotes the perfect lattice.

4.2. Multiaxial yield response of the imperfect lattice

The sensitivity of the shape of the yield surface to imperfection is now explored. We anticipate a major change in the shape of yield surface in stress space that contains the hydrostatic limit: σ_{hy} drops much more sharply with increasing ζ than does σ_Y or τ_Y. To illustrate this, we plot the yield surface in axisymmetric stress space ($\sigma_{xx} = \sigma_{yy}, \sigma_{zz}$) in Fig. 7(b) for $\zeta = 0$ and $\zeta = 1.76$. The yield surface becomes much less elongated with increasing ζ. This has been noted previously for irregular hexagonal honeycombs, see for example (Chen et al., 1999). In contrast, for stress states that generate a bending response of the perfect lattice, there is only a very minor change in behaviour when nodal imperfections are introduced. Consequently, the yield surfaces for the plane stress loading (σ_{xx}, σ_{yy}) and for shear loading (σ_{xy}, σ_{xz}) are little changed when ζ is increased from 0 to 1.76, see Figs. 4(b) and 6(b).

5. Analytical formula for the multiaxial yield function

For practical applications, it is beneficial to obtain an expression for the macroscopic multiaxial yield behaviour of the gyroid lattice in analytic form. We make two attempts to do this and restrict our attention to the practical case of the imperfect lattice. It is clear from Fig. 9(b) that the hydrostatic and uniaxial yield strengths converge to a constant values for $\zeta > 1.5$, and so the multiaxial response for $\zeta = 1.76$ can be taken as representative of that for large imperfection. All FE simulations in this section are performed for $\bar{\rho} = 3.3\%$.

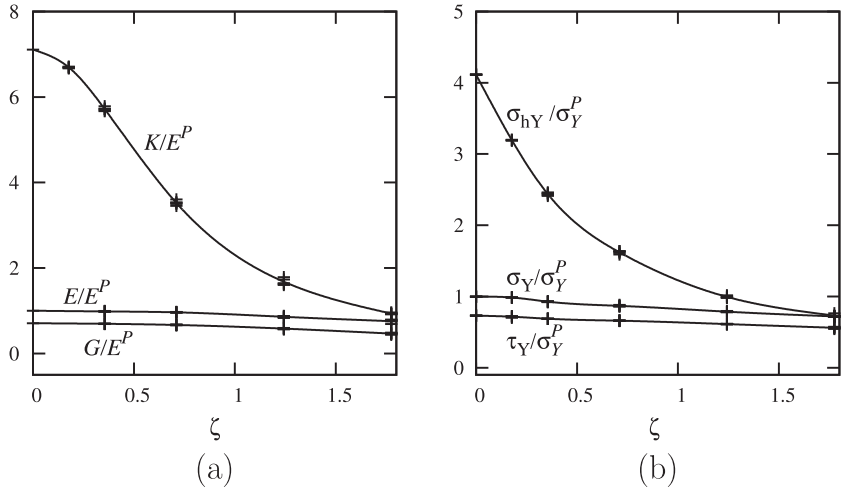

Fig. 9. (a) Elastic constants and (b) yield strengths of the $\bar{\rho} = 3.3\%$ gyroid lattice as a function of the imperfection magnitude ζ. The superscript P refers to the perfect lattice.

5.1. Case A – the Deshpande–Fleck (D–F) foam model

First, we attempt to curve fit the D–F isotropic metal foam model (Deshpande and Fleck, 2000). Recall that the D–F yield function is of the form

$$\sigma_e^2 + \alpha^2 \sigma_h^2 = c^2, \tag{16}$$

where σ_e is the von Mises effective stress, σ_h is the hydrostatic stress and (α, c) are material constants. Upon fitting Eqn (16) to the (σ_{hY}, σ_Y), data of Fig. 9(b) at $\zeta = 1.76$, we obtain $\alpha = 3/(2\sqrt{2})$ and $c = \alpha\sigma_Y$, where $\sigma_Y = 0.315\sigma_S\bar{\rho}^{3/2}$ is the uniaxial yield strength of the imperfect lattice. The accuracy of the resulting D–F yield function is acceptable for the axisymmetric case, see Fig. 10(a). A second assessment is made in (σ_h, σ_{xy}) space, see Fig. 10(b). The loading is now $\sigma_{xx} = \sigma_{yy} = \sigma_{zz} = \sigma_h$ along with σ_{xy}. In this subspace, the D–F foam model is conservative by at most 20%, with most deviation occurring for the state of pure shear. Recall that the imperfect gyroid is not isotropic, and thus an isotropic description entails an approximation. We proceed to improve the accuracy of the analytical description, but at the cost of more fitting parameters.

5.2. Case B – extension of Hill's anisotropic yield function

In order to obtain an improved description of the yield behaviour we use the modified Hill's yield criterion, as proposed by Deshpande et al. (2001):

$$A(\sigma_{xx} - \sigma_{yy})^2 + B(\sigma_{yy} - \sigma_{zz})^2 + C(\sigma_{zz} - \sigma_{xx})^2 + D\sigma_{xy}^2 + E\sigma_{yz}^2 + F\sigma_{xz}^2 + G\sigma_h^2 = 1, \tag{17}$$

where the constants A to G are obtained by curve fitting, as follows. Consider the imperfect lattice ($\zeta = 1.76$). The constants A to G are obtained by considering the following loading states:

i. the hydrostatic yield strength σ_{hY} is almost identical to the uniaxial yield strength σ_Y at $\zeta = 1.76$, see Fig. 9(b). Consequently, $G = 1/\sigma_Y^2$.
ii. under uniaxial loading in the x, y or z directions, the uniaxial strength σ_Y is obtained. Consequently, $A = B = C = 4/(9\sigma_Y^2)$.
iii. under shear loading in xz, yz or xy plane, we note from Fig. 9(b), that the shear strength $\tau_Y = 0.77\sigma_Y$. Consequently, $D = E = F = 1.69/\sigma_Y^2$.

The yield surface, as defined by (17), is compared against simulations in Fig. 10. The anisotropic yield criterion is more accurate than the isotropic yield criterion for stress states far from the hydrostatic limit.

We note in passing that the anisotropic yield function collapses to the D–F surface in the absence of the shear stress components $(\sigma_{xy}, \sigma_{xz}, \sigma_{yz})$. Thus, for axisymmetric loading $(\sigma_{xx} = \sigma_{yy}, \sigma_{zz})$, it offers no improvement over the isotropic version, see Fig. 10(a).

6. Case study: the gyroid thin films

The above yield criteria can be used immediately for design purposes. Consider, for example, the application of the gyroid lattice to electronic displays. A thin film of gyroid lattice is bonded to a glass substrate, and when infiltrated with a suitable electrolyte, it functions as an electrochromic device (Scherer et al., 2012). The gyroid is taken to be imperfect, with $\zeta = 1.76$. In service, the gyroid film may yield due to thermal expansion mismatch with the underlying substrate or due to swelling of the lattice caused by the electrochemical reactions within the electrochromic device. We explore this issue for gyroids with $\bar{\rho} < 4\%$. For simplicity we assume that one of the cubic directions of the gyroid lattice is aligned with the unit normal to the surface, and arbitrarily take this to be the z direction.

First, consider the thermal problem. Impose a uniform temperature change ΔT to the film and substrate, from the initial, stress-free configuration. The components of the mismatch strain are $\epsilon_{xx}^* = \epsilon_{yy}^* = \Delta\alpha\Delta T$, where $\Delta\alpha = \alpha_f - \alpha_s$ is the difference in the coefficient of thermal expansion between the film α_f[2] and substrate α_s. The thermal stresses due to this mismatch is $\sigma_{xx} = \sigma_{yy} = -E\Delta\alpha\Delta T/(1-\nu)$, where E is the uniaxial modulus and ν is the Poisson ratio of the lattice. From the data shown in Fig. 9(a), we can assume that $E = 0.319E_S\bar{\rho}^2$ and $\nu = 1/3$. This state of stress is marked by points A in Fig. 10(a), for positive and negative values of $\Delta\alpha\Delta T$. Both versions of the yield functions as derived in the previous section imply that the maximum allowable temperature change without inducing yield is $\Delta T = 0.856\epsilon_S(1-\nu)/\Delta\alpha\sqrt{\bar{\rho}}$, where ϵ_S is the yield strain of the solid material. It is instructive to compare this with the maximum allowable value of ΔT of a solid film, without inducing yielding. Consider a solid film that is made from the same material as the lattice, bonded to the substrate, and subjected to the

[2] α_f of the gyroid lattice is equal to the coefficient of thermal expansion of the solid it is made from.

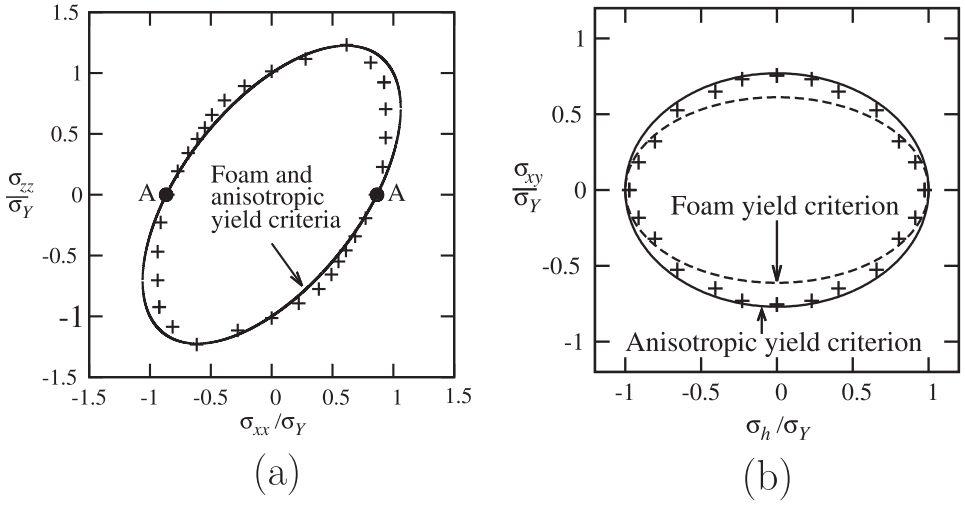

Fig. 10. Comparison between the isotropic foam and anisotropic yield criteria for (a) axisymmetric loading and (b) in (σ_h, σ_{xy}) space. '+' Symbols refer to finite element simulations of a imperfect lattice (one realization). In (a), the stress state in a gyroid film subject to thermal stress is marked by label A.

thermal mismatch strain as mentioned above. The thermal stresses due to this mismatch is $\sigma_{xx} = \sigma_{yy} = -E_S\Delta\alpha\Delta T/(1-\nu_S)$, where E_S and ν_S are the Young's modulus and Poisson ratio of the solid film, respectively. Assuming that the solid film yields according to the von Mises yield criterion, we have $\Delta T = \epsilon_S(1-\nu_S)/\Delta\alpha$. In contrast, the allowed ΔT scales as $\bar{\rho}^{-1/2}$ for the gyroid film. We conclude that the gyroid can undergo a larger ΔT than its parent solid. To emphasize this, we plot in Fig. 11(a) the allowable ΔT values for solid and gyroid films made from different materials on a substrate of silica glass $\alpha_s = 0.55 \times 10^{-6}\,^{\circ}\mathrm{C}^{-1}$ (Ashby, 2005) and $\nu_S = 1/3$. The results of Fig. 11(a) are obtained using the material properties listed in Table 2. We note that for all film materials and $\bar{\rho}$ values considered here, the gyroid lattice can sustain a larger ΔT without yielding compared to the solid material.

Second, consider the possibility of yielding of the gyroid lattice when it is used as an electrochromic device. During operation of the electrochromic device, intercalation of ions from the electrolyte into the struts of the gyroid lattice takes place (Scherer et al., 2012), and this may result in swelling of the lattice. The components of mismatch strain are $\epsilon^*_{xx} = \epsilon^*_{yy} = \epsilon_v/3$, where the stress-free volumetric strain ϵ_v depends upon the concentration of intercalating species in the struts (Zhang et al., 2007). The stress due to constrained swelling is $\sigma_{xx} = \sigma_{yy} = -E\epsilon_v/[3(1-\nu)]$. Now apply either of the analytical functions in (16) and (17) for the imperfect gyroid. We deduce that ϵ_v is given by $\epsilon_v = 2.56\epsilon_S(1-\nu)/\sqrt{\bar{\rho}}$. For comparison, consider the intercalation of ions into a solid film, made of the same material as the lattice, and bonded to the substrate. When subjected to the same mismatch strain as mentioned above, the in-plane stress due to volumetric swelling is $\sigma_{xx} = \sigma_{yy} = -E_S\epsilon_v/[3(1-\nu_S)]$. Upon applying the von Mises yield criterion we obtain $\epsilon_v = 3\epsilon_S(1-\nu_S)$. In contrast, the allowable ϵ_v scales as $\bar{\rho}^{-1/2}$ for the gyroid film. A summary of the allowable volumetric strain is shown in Fig. 11(b) for both solid (assuming $\nu_S = 1/3$) and gyroid films, made from the same parent materials as introduced in Table 2. Again, the gyroid lattice outperforms

Table 2
Properties of materials used to obtain the results in Fig. 11.

Film material	ϵ_S (%)	α_f ($10^{-6}\,^{\circ}\mathrm{C}^{-1}$)
Copper (Ashby, 2005)	0.026	17.1
Nickel (Ashby, 2005)	0.037	13.3
Platinum (Smithells, 1984)	0.053	9.2
Cobalt (Smithells, 1984)	0.117	12.3

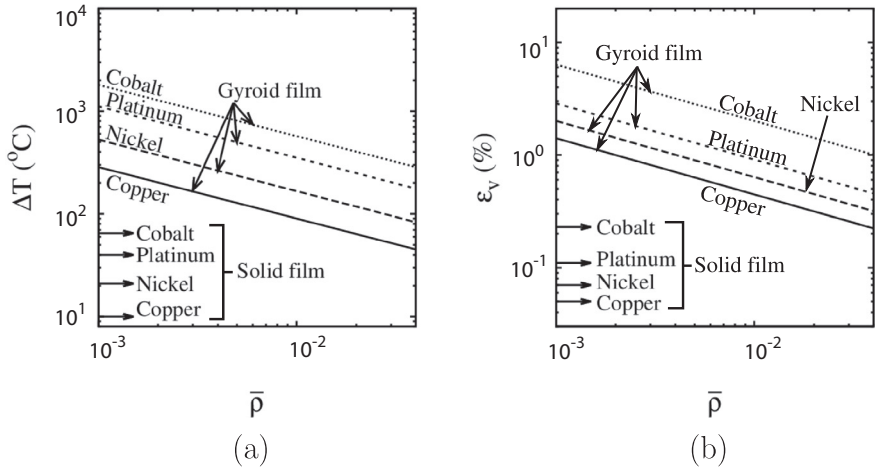

Fig. 11. (a) Maximum allowed temperature change ΔT (to avoid plastic yielding) for solid and gyroid thin films made from different materials. The material properties used are given in Table 2. (b) Maximum allowed volume expansion ϵ_v (to avoid plastic yielding) for solid and gyroid thin films made from different materials.

Table 3
Comparison of uniaxial modulus E and uniaxial yield strength σ_Y for open-celled foams, gyroid lattice and octet truss lattice.

Lattice type	E/E_S	σ_Y/σ_S
Open-celled foams (Gibson and Ashby, 1997)	$\bar{\rho}^2$	$0.3\bar{\rho}^{3/2}$
Imperfect gyroid lattice ($\xi = 1.76$)	$0.319\ \bar{\rho}^2$	$0.315\bar{\rho}^{3/2}$
Octet truss lattice (Fleck et al., 2010)	$0.3\bar{\rho}$	$0.3\bar{\rho}$

the solid thin films. Thus, a gyroid lattice shows promise for thin film applications. Thermal conductivity is an important parameter in such applications and this is analysed in Appendix B.

7. Comparison with other cellular materials

In this section we compare the uniaxial modulus E and the uniaxial yield strength σ_Y of the imperfect gyroid lattice (with $\xi = 1.76$) with that of open-celled foams and octet truss lattice. The properties of the foams are obtained from Gibson and Ashby (1997) and that of the octet truss lattice are obtained from Fleck et al. (2010). The comparison is shown in Table 3. Both the gyroid lattice and the open-celled foams are bending dominated structures. Hence, their uniaxial modulus scales as $\bar{\rho}^2$ and the uniaxial yield strength scales as $\bar{\rho}^{3/2}$. In contrast, since the octet truss lattice is a stretching dominated structure, the scaling of the uniaxial modulus and yield strength is linear with $\bar{\rho}$. Hence, for a given relative density and parent solid, the stiffness and strength of gyroid and open-celled foams are similar, but much lower than that of the octet truss lattice. For example at $\bar{\rho} = 0.04$, the modulus and strength of the gyroid are a factor of 0.043 and 0.21, respectively, less than that of the octet truss lattice.

8. Concluding remarks

1. The perfect gyroid lattice has cubic symmetry and deforms by bar stretching under macroscopic hydrostatic stressing. Consequently, its macroscopic bulk modulus K and hydrostatic strength σ_{hY} scale linearly with the relative density $\bar{\rho}$. Under all other stress states, the bars of the lattice bend. Consequently, the uniaxial modulus and shear modulus (aligned with the cubic axes) scale as $\bar{\rho}^2$; and the uniaxial yield strength σ_Y and shear yield strength τ_Y scale as $\bar{\rho}^{3/2}$.

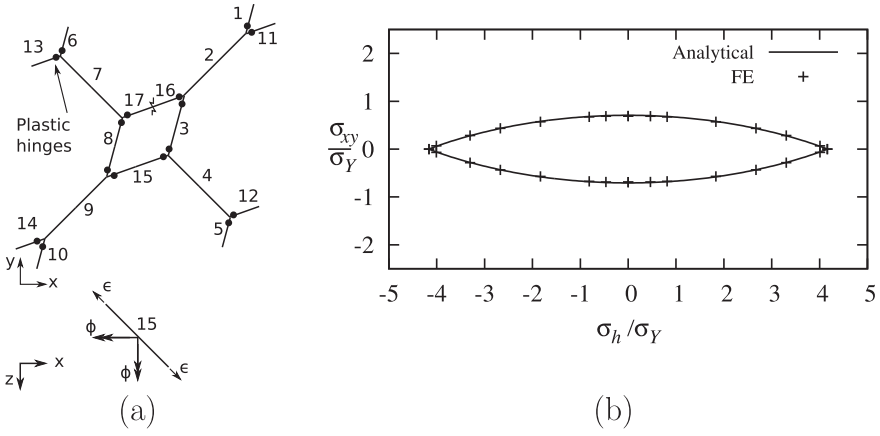

Fig. 12. Yield behaviour in (σ_h, σ_{xy}) space. (a) Deformed geometry and location of plastic hinges for the collapse mode. (b) Comparison of analytical yield surface and FE simulation.

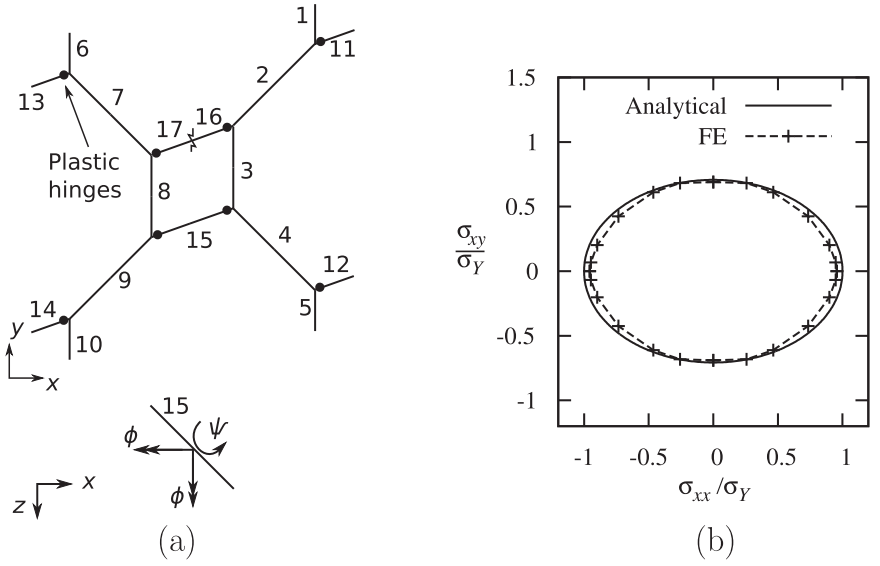

Fig. 13. Yield behaviour in $(\sigma_{xx}, \sigma_{xy})$ space. (a) Deformed geometry and location of plastic hinges for the collapse mode. (b) Comparison of analytical yield surface and FE simulation.

2. Imperfections, in the form of a random repositioning of the nodes of the lattice, lead to a severe knock-down in the hydrostatic properties (elastic and plastic), but to a negligible change in deviatoric properties. This is traced to the fact that bar bending occurs for all stress states including hydrostatic. A similar behaviour has been noted previously by Chen et al. (1999) for the regular hexagonal honeycomb.
3. The yield surface of the perfect and imperfect gyroid has been determined for a broad range of stress states. A small geometric imperfection reduces the hydrostatic strength to a value comparable with the uniaxial strength. The yield surface of the imperfect lattice ($\zeta = 1.76$) can be fitted by a quadratic yield criterion, such as Deshpande–Fleck isotropic foam model or the modified Hill anisotropic yield criterion. The anisotropic criterion is more accurate, but it requires additional calibration.
4. The thermo-mechanical properties of a gyroid thin film upon an elastic substrate are assessed for application to electronic displays. It is demonstrated that the lattice can sustain a relatively large temperature excursion and swelling strain without inducing yield, when compared to a solid film made from the same material.

Appendix A. Additional multiaxial yield surfaces for perfect lattice

In this section we analyse the multiaxial yield response of the perfect gyroid lattice in stress spaces (σ_h, σ_{xy}) and $(\sigma_{xx}, \sigma_{xy})$, where σ_h is the hydrostatic stress. The lattice is considered to be aligned with Cartesian (x, y, z) axes (see Fig. 2) and and modelled as beams. A set of kinematically admissible collapse modes are postulated and the collapse stress is determined for each using upper bound theorem of plasticity. Elasto-plastic FE simulations are performed using periodic unit cell to identify the collapse modes. The accuracy of the upper bound prediction is verified by comparing against FE results.

A.1. Yield surface in (σ_h, σ_{xy}) space

The yield surface in (σ_h, σ_{xy}) space is now analysed. FE simulations are performed on a periodic unit cell by applying a combination of σ_{xy} and $\sigma_{xx} = \sigma_{yy} = \sigma_{zz} = \sigma_h$, in proportional stressing, with all other $\sigma_{ij} = 0$. The collapse surface and collapse mode as obtained from FE simulations are shown in Fig. 12. The single collapse mode is characterised by two degrees of freedom: rotation and stretching of struts at the nodes.

The struts 11, 13 and 15 rotate by $-\phi\boldsymbol{e}_x + \phi\boldsymbol{e}_z$, the struts 12, 14, 16 and 17 rotate by $\phi\boldsymbol{e}_x + \phi\boldsymbol{e}_z$, the struts 1, 8 and 5 rotate by $\phi\boldsymbol{e}_y - \phi\boldsymbol{e}_z$ and the struts 6, 3 and 10 rotate by $-\phi\boldsymbol{e}_y - \phi\boldsymbol{e}_z$. These struts also stretch axially by $\epsilon L/2$ at the plastic hinge. Here, ϵ is a dimensionless kinematic variable characterising the degree of axial stretch. The non-zero macroscopic plastic strains are $\epsilon^p_{xx} = \epsilon/2, \epsilon^p_{yy} = \epsilon/2, \epsilon^p_{zz} = \epsilon$ and $\epsilon^p_{xy} = 2\phi$. Note that the extension of the struts causes a volumetric strain and the rotation of struts causes the shear strain. The total work done by the external forces is given by

$$W_{\text{ext}}(\epsilon, \phi) = [\sigma_{xy}(2\phi) + \sigma_h(2\epsilon)]a^3. \tag{A.1}$$

The energy dissipated can be written as

$$W_{\text{plas}}(\epsilon, \phi) = 16\frac{\epsilon L}{2}P_p(\xi) + 16\phi M_p(\xi). \tag{A.2}$$

Refer to Section 3.3 for the definitions of $P_p(\xi)$ and $M_p(\xi)$. Now equate W_{ext} and W_{plas} and note that ϕ and ϵ are independent; this leads to the yield criterion

$$\begin{aligned}\sigma_{xy} &= \pm\frac{\sigma_Y}{\sqrt{2}}\left(1-\xi^2\right)^{3/2},\\ \sigma_h &= \frac{3}{4}\left(\frac{L}{d}\right)\sigma_Y\left(\sin^{-1}\xi + \xi\sqrt{1-\xi^2}\right),\end{aligned} \tag{A.3}$$

in parametric form, where $-1 \leqslant \xi \leqslant 1$. The upper bound solution is compared with FE simulations in Fig. 12(b). The close agreement between the FE and upper bound solution implies that the postulated collapse mode is exact.

A.2. Yield surface in $(\sigma_{xx}, \sigma_{xy})$ space

The yield surface in $(\sigma_{xx}, \sigma_{xy})$ space is analysed next. To identify the collapse modes, FE simulations are performed by imposing a proportional stressing such that $\sigma_{xx} = \lambda\sigma_{xy}$, and all other $\sigma_{ij} = 0$. The results are shown in Fig. 13, along with the postulated collapse mode. The collapse mode consists of struts rotating with two degrees of freedom ϕ and ψ about the nodes. For example, the rotation of strut 15 is shown in the $x - z$ plane in Fig. 13(a).

The struts 11, 13 and 15 rotate by $-\phi\boldsymbol{e}_x + \psi\boldsymbol{e}_y + \phi\boldsymbol{e}_z$ and the struts 12, 14, 16 and 17 rotate by $\phi\boldsymbol{e}_x - \psi\boldsymbol{e}_y + \phi\boldsymbol{e}_z$. This leads to the following macroscopic plastic strains: $\epsilon^p_{xx} = -\epsilon^p_{yy} = \psi/2$ and $\epsilon^p_{xy} = \phi$. Note that the shear strain is caused by the rotation about x and z axes, whereas the axial strain is caused by the rotation about y direction. The work done by the external forces is

$$W_{\text{ext}} = a^3\left(\sigma_{xx}\frac{\psi}{2} + \sigma_{xy}\phi\right). \tag{A.4}$$

The equivalent rotation of the plastically yielding struts is $\sqrt{\psi^2 + 2\phi^2}$, so that the energy dissipated at the eight plastic hinges is

$$W_{\text{plas}} = 8M_p\sqrt{\psi^2 + 2\phi^2}. \tag{A.5}$$

After equating the work done by external forces to the dissipation energy we get the yield criterion as

$$\sigma^2_{xx} + 2\sigma^2_{xy} = \sigma^2_Y. \tag{A.6}$$

The yield surfaces calculated from the above analytical expression and from FE simulations are compared in Fig. 13(b). The discrepancy is attributed to the differences between the exact and postulated collapse modes.

Appendix B. Thermal conductivity of gyroid lattice

The effective thermal conductivity of the gyroid lattice is an important parameter in thin film applications of the gyroid lattice. Heat can be transferred across the lattice by four mechanisms (Gibson and Ashby, 1997): (1) conduction through the struts (2) conduction through any in-filling medium (when present), (3) convection and (4) radiation. The effective thermal conductivity of the perfect gyroid is now calculated using the beam model of the gyroid, assuming that heat transfer is entirely governed by conduction through the beams.

The effective thermal conductivity k is identical along each cubic direction (Nye, 2004). Align the lattice with the Cartesian (x, y, z) axes. Consider a unit cell of side dimension a, and specify a temperature difference ΔT across the cell in y direction. Using Fourier's law, the heat transferred in y direction can be written as

$$Q = a^2 k\frac{\Delta T}{a},$$

where k is the effective thermal conductivity of the lattice. Heat flow in the y direction is due to the conduction along two beam paths: the bars labelled as (i) 1, 2, 3, 4 and 5, and (ii) 6, 7, 8, 9

and 10, see Fig. 2. The total length of each of these paths is $4L$. Hence, Q can also be written as $Q = (\pi/2)d^2 k_S(\Delta T/4L)$, where k_S is the thermal conductivity of the solid material. By equating the above two expressions for Q, we obtain

$$k = \frac{1}{3}\bar{\rho}k_S,$$

where $\bar{\rho}$ is the relative density of the lattice.

Now consider the imperfect lattice, where the nodes of the lattice are displaced by ζd in random direction. The average length of beams does not change, and so the effective thermal conductivity of the imperfect gyroid lattice is equal to that of the perfect lattice.

References

Almsherqi, Z., Margadant, F., Deng, Y., 2012. A look through lens cubic mitochondria. Interface Focus.

Ashby, M.F., 2005. Material Selection in Mechanical Design. Elsevier.

Ashby, M.F., 2006. The properties of foams and lattices. Philos. Trans. R. Soc. A 364, 15–30.

Chen, C., Lu, T., Fleck, N., 1999. Effect of imperfections on the yielding of two-dimensional foams. J. Mech. Phys. Solids 47, 2235–2272.

Christensen, R., 2000. Mechanics of cellular and other low-density materials. Int. J. Solids Struct. 37 (1), 93–104.

Cote, F., Deshpande, V., Fleck, N., Evans, A., 2004. The out-of-plane compressive behavior of metallic honeycombs. Mater. Sci. Eng.: A 380, 272–280.

Deshpande, V., Fleck, N., 2000. Isotropic constitutive models for metallic foams. J. Mech. Phys. Solids 48 (6), 1253–1283.

Deshpande, V., Ashby, M., Fleck, N., 2001. Foam topology: bending versus stretching dominated architectures. Acta Mater. 49 (6), 1035–1040.

Deshpande, V., Fleck, N., Ashby, M., 2001. Effective properties of the octet-truss lattice material. J. Mech. Phys. Solids 49 (8), 1747–1769.

Fleck, N.A., Qiu, X., 2007. The damage tolerance of elasticbrittle, two-dimensional isotropic lattices. J. Mech. Phys. Solids 55 (3), 562–588.

Fleck, N.A., Deshpande, V.S., Ashby, M.F., 2010. Micro-architectured materials: past, present and future. Philos. Trans. R. Soc. A 466, 2495–2516.

Gibson, L.J., Ashby, M.F., 1997. Cellular Solids – Structure and Properties. Cambridge University Press.

Jacobsen, A., Barvosa-Carter, W., Nutt, S., 2007. Micro-scale truss structures formed from self-propagating photopolymer waveguides. Adv. Mater. 19 (22), 3892–3896.

Kapfer, S.C., Hyde, S.T., Mecke, K., Arns, C.H., Schrder-Turk, G.E., 2011. Minimal surface scaffold designs for tissue engineering. Biomaterials 32 (29), 6875–6882 <http://www.sciencedirect.com/science/article/pii/S0142961211006776>.

Luzzati, V., Spegt, P.A., 1967. Polymorphism of lipids. Nature 215 (5102), 701–704.

Matsen, M.W., Bates, F.S., 1996. Unifying weak- and strong-segregation block copolymer theories. Macromolecules 29 (4), 1091–1098.

Michielsen, K., Kole, J.S., 2003. Photonic band gaps in materials with triply periodic surfaces and related tubular structures. Phys. Rev. B 68, 115107 <http://link.aps.org/doi/10.1103/PhysRevB.68.115107>.

Michielsen, K., Stavenga, D.G., 2008. Gyroid cuticular structures in butterfly wing scales: biological photonic crystals. J. R. Soc., Interface 5, 84–94.

Nye, J., 2004. Physical Properties of Crystals. Oxford University Press.

Papka, S.D., Kyriakides, S., 1994. In-plane compressive response and crushing of honeycomb. J. Mech. Phys. Solids 42 (10), 1499–1532.

Queheillalt, D.T., Wadley, H.N., 2005. Cellular metal lattices with hollow trusses. Acta Mater. 53 (2), 303–313.

Saranathan, V., Osuji, C.O., Mochrie, S.G.J., Noh, H., Narayanan, S., Sandy, A., Dufresne, E.R., Prum, R.O., 2010. Structure, function, and self-assembly of single network gyroid (I4132) photonic crystals in butterfly wing scales. Proc. Natl. Acad. Sci. 107 (26), 11676–11681.

Scherer, M., 2009. Nanostructured materials via self-assembled templates (Master's thesis). University of Konstanz.

Scherer, M.R.J., Li, L., Cunha, P.M.S., Scherman, O.A., Steiner, U., 2012. Enhanced electrochromism in gyroid-structured vanadium pentoxide. Adv. Mater. 24 (9), 1217–1221.

Silva, M.J., Hayes, W.C., Gibson, L.J., 1995. The effects of non-periodic microstructure on the elastic properties of two-dimensional cellular solids. Int. J. Mech. Sci. 37 (11), 1161–1177.

Smithells, C.J., 1984. Metals Reference Book.

Triantafyllidis, N., Schraad, M., 1998. Onset of failure in aluminum honeycombs under general in-plane loading. J. Mech. Phys. Solids 46 (6), 1089–1124.

Yan, C., Hao, L., Hussein, A., Raymont, D., 2012. Evaluations of cellular lattice structures manufactured using selective laser melting. Int. J. Mach. Tools Manuf. 62, 32–38.

Zhang, X., Shyy, W., Sastry, A.M., 2007. Numerical simulation of intercalation-induced stress in li-ion battery electrode particles. J. Electrochem. Soc. 154 (10), A910–A916.

Zhu, H., Hobdell, J., Windle, A., 2000. Effects of cell irregularity on the elastic properties of open-cell foams. Acta Mater. 48 (20), 4893–4900.